APL Photonics

Ultra-broadband mid-infrared Ge-on-Si waveguide polarization rotator

Cite as: APL Photonics 5, 026102 (2020); https://doi.org/10.1063/1.5134973
Submitted: 04 November 2019 . Accepted: 29 January 2020 . Published Online: 18 February 2020

Kevin Gallacher, Ross W. Millar, Ugne Griškevičiūtė, Martin Sinclair, Marc Sorel, Leonetta Baldassarre, Michele Ortolani, Richard Soref, and Douglas J. Paul

Ultra-broadband mid-infrared Ge-on-Si waveguide polarization rotator

Cite as: APL Photon. 5, 026102 (2020); doi: 10.1063/1.5134973
Submitted: 4 November 2019 • Accepted: 29 January 2020 •
Published Online: 18 February 2020

Kevin Gallacher,[1,a] Ross W. Millar,[1] Ugne Griškevičiūtė,[1] Martin Sinclair,[1] Marc Sorel,[1] Leonetta Baldassarre,[2] Michele Ortolani,[2] Richard Soref,[3] and Douglas J. Paul[1]

AFFILIATIONS

[1]University of Glasgow, James Watt School of Engineering, Rankine Building, Oakfield Avenue, Glasgow G12 8LT, United Kingdom
[2]Dipartimento di Fisica, Universita di Roma La Sapienza, Piazzale Aldo Moro 5, I-00185 Roma, Italy
[3]Engineering Program, University of Massachusetts at Boston, Boston, Massachusetts 02125, USA

[a)]Author to whom correspondence should be addressed: kevin.gallacher@glasgow.ac.uk

ABSTRACT

The design, modeling, micro-fabrication, and characterization of an ultra-broadband Ge-on-Si waveguide polarization rotator are presented. The polarization rotator is based on the mode evolution approach where adiabatic symmetric and anti-symmetric tapers are utilized to convert from the fundamental transverse magnetic to electric mode. The device is shown to be extremely fabrication tolerant and simple to fabricate. The fabricated devices demonstrate a polarization extinction ratio of ≥15 dB over a 2 μm bandwidth (9–11 μm wavelength) with an average insertion loss of <1 dB, which is an order of magnitude improvement compared to previously demonstrated devices. This device will provide polarization flexibility when integrating quantum cascade lasers on-chip for mid-infrared waveguide molecular spectroscopy.

I. INTRODUCTION

The mid-infrared (MIR) spectral region is of significant interest for several applications such as security,[1] healthcare,[2] drug identification,[3] and environmental monitoring.[4,5] This is due to how chemical compounds can be identified through their unique vibrational modes, which absorb in the molecular "fingerprint" region (6.7–20 μm wavelength).[6] An integrated waveguide molecular spectrometer would significantly reduce the size and cost compared to commercially available spectrometers.[7] A waveguide spectrometer requires the integration of a source and detector along with the passive waveguides for sensing. There have been several waveguide platforms that have been demonstrated in the fingerprint region such as chalcogenide glasses,[8] GaAs,[9] SiGe,[10,11] and Ge-on-Si.[12,13] Ge-on-Si is a promising platform since it is Si foundry compatible and optically transparent up to ~15 μm wavelength.[14] There have been many optical components that have been demonstrated including plasmonic amplifiers,[15,16] light emitters,[17] third harmonic generators,[18] quantum well infrared photodetectors,[19] and microbolometers.[20]

A potential candidate for the source is a quantum cascade laser (QCL), which has recently demonstrated significant tuning ranges.[21] By integrating several QCLs on-chip[22] with tunable waveguide resonators,[23] this would enable scanning across many molecular absorption lines with high power and would compensate for a non-cryogenically cooled detector (see Fig. 1). This would provide an alternative architecture compared to realizing an integrated Fourier-transform spectrometer.[24–26]

One drawback of using a QCL is the emitted vertical polarization that will only couple to transverse magnetic (TM) guided modes. We recently demonstrated Ge-on-Si waveguides operating up to 11 μm wavelength with low propagation losses (~1 dB/cm).[27] The key to achieving this was guiding with a transverse electric (TE) mode to minimize interactions with the Si substrate that is non-transparent past 8 μm wavelength. Figure 2(a) shows the experimentally measured absorption coefficient for Si and its corresponding effect on the simulated propagation loss for the fundamental TE and TM modes in a 2 μm thick Ge-on-Si rib waveguide. The TE mode also provides the benefit of smaller bending radii [see the inset of Fig. 2(a)] and an increased modal overlap for sensing [see

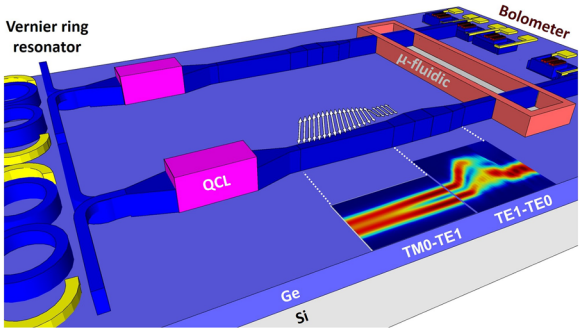

FIG. 1. A schematic diagram of an envisaged integrated waveguide molecular spectrometer. Key components include the passive Ge-on-Si waveguides, broadband quantum cascade lasers, Vernier ring resonator tuning cavities, bolometer detectors, micro-fluidics, and a polarization rotator.

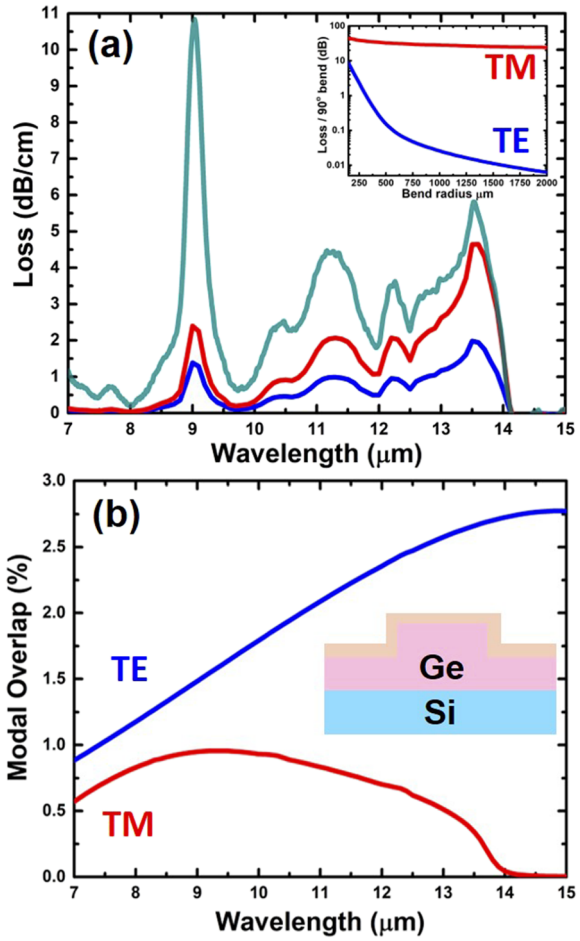

FIG. 2. (a) The Si absorption (cyan) and the modeled waveguide loss caused by the modal overlap of the fundamental TE (blue) and TM (red) modes in a 8 μm wide, 2 μm thick Ge-on-Si rib waveguide with Si. The inset shows the modeled bending loss for a 90° bend at 13.5 μm wavelength. (b) The modeled modal overlap vs wavelength for the TE and TM modes for sensing an analyte that covers all waveguide surfaces.

Fig. 2(b)].[28] To enable TE operation with integrated QCLs, the most obvious strategy would be to utilize a polarization rotator.

There has been substantial research into developing waveguide polarization rotators for creating polarization-insensitive photonic circuits on the silicon-on-insulator (SOI) platform at telecommunication wavelengths.[29] The key figures of merit (FOM) usually presented are the polarization extinction ratio (PER), insertion loss (IL), and operational bandwidth. To date, the largest operational bandwidths demonstrated have been ≤200 nm with an IL ≤1 dB and a PER ≥10 dB.[30] There has been limited investigation into migrating a waveguide polarization rotator to the MIR, where the majority of the work has been predominately simulation[31,32] and where there have been two recent experimental demonstrations below 6.15 μm wavelength.[33,34] Here, we demonstrate the design, modeling, microfabrication, and characterization of a Ge-on-Si waveguide polarization rotator operating between 9 μm and 11 μm wavelengths with an average IL <1 dB and a PER ≥15 dB.

II. DESIGN AND MODELING

There are typically three main strategies employed to realize waveguide polarization rotation devices: rotator waveguides,[35] cross polarization coupling,[36] and mode evolution.[37] The simplest to implement is the mode evolution approach, where an adiabatic taper can efficiently convert polarization between a TM and TE mode.[38] This approach has the advantage that it is normally fabrication tolerant and only requires a single lithography and etch step, and for these reasons, this is the approach that is utilized in this work.

A. Ge-on-Si mode hybridization

The main requirements to utilize the mode evolution approach are that the waveguide is birefringent and has a cross-sectional asymmetry so that mode hybridization occurs.[39] These requirements are met by a 2 μm thick Ge heterolayer on Si etched by 1 μm to form a rib waveguide that is air clad. A finite-difference eigenmode solver (Lumerical) was used to calculate the effective indices of the supported eigenmodes vs the waveguide width. It is clear from Fig. 3(a) that the supported TE0 and TM0 modes are highly birefringent ($\Delta n \sim 0.075$) and there is anti-crossing between the TM0 and TE1 modes at a waveguide width of ~7.9 μm, which is indicative of mode hybridization. The mode hybridization can be confirmed by analyzing the polarization ratio (γ_x), which is defined as the ratio of the non-dominant to dominant field component of the fundamental mode, as follows:[40]

$$\gamma_x = \frac{\int_S |E_x^2| dxdy}{\int_S |E_x^2| dxdy + \int_S |E_y^2| dxdy}. \quad (1)$$

For non-hybridized modes, γ_x is ≈0 and 100 for TM and TE modes, respectively. When the modes are hybridized, the electric field components, E_x and E_y, become comparable (i.e., 50%). Figure 3(b) represents the calculated γ_x of the supported TM0 and TE1 modes of the Ge-on-Si rib waveguides at 8 μm and 11 μm wavelengths. This wavelength range is specifically chosen since it matches the bandwidth of a broadly tunable QCL and is accessible with the experimental setup. It is clear that the anti-crossing identified is indeed a point where the TM0 and TE1 modes are fully hybridized.

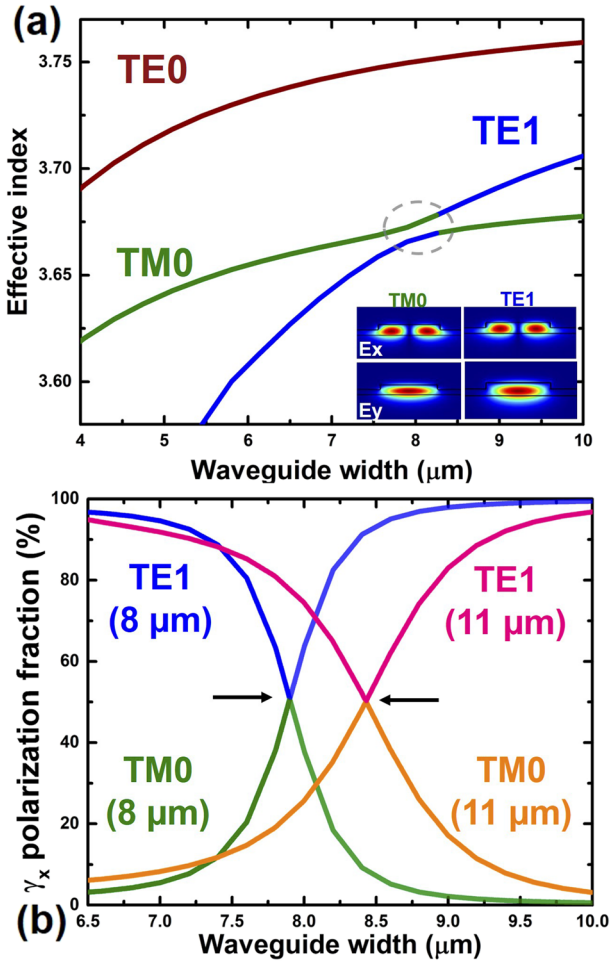

FIG. 3. (a) The calculated effective modal indices vs the waveguide width for the supported modes in a Ge-on-Si rib waveguide with a 1 μm partial etch at 8 μm wavelength. The inset shows the E_x and E_y electric field profiles of the modes at the anti-crossing point. (b) The calculated mode polarization ratio, $\gamma_x = E_x^2/(E_x^2 + E_y^2)$, of the TM0 and TE1 mode vs waveguide width at 8 μm and 11 μm wavelengths. The arrows are used to highlight the 50% mode hybridization point for each wavelength.

What is particularly interesting in Fig. 3(b) is that only an ~0.5 μm waveguide width change is required for mode hybridization to occur between 8 μm and 11 μm wavelengths. Since hybridization is confirmed between the TM0 and TE1 modes, an adiabatic taper can be used to provide polarization conversion.

B. Broadband TM0 to TE1 mode conversion

The attainment of efficient polarization conversion over the 8–11 μm wavelength range requires a taper design that has an input and output width that spans the mode hybridization regions identified in Fig. 3(b). An eigenmode expansion (EME) solver was used to model a linear taper with an input and output width of 7.7 μm and 8.7 μm, respectively. The calculated TM0 to TE1 polarization

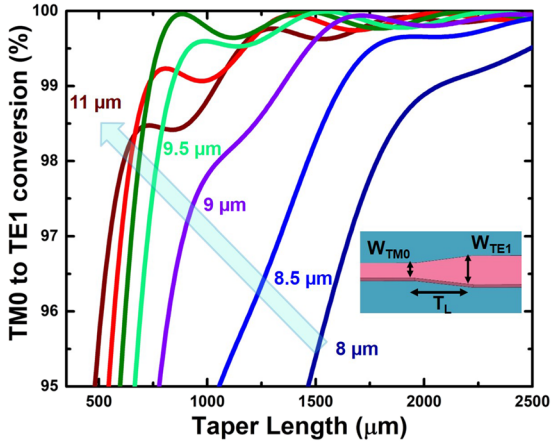

FIG. 4. The modeled TM0 to TE1 mode conversion efficiency vs taper length (T_L) for a Ge-on-Si rib waveguide that is linearly tapered from an input width (W_{TM0}) of 7.7 to an output width (W_{TE1}) of 8.7 μm. The calculated wavelengths consist of 8–11 μm in 0.5 μm increments.

conversion efficiency (PCE) for different wavelengths vs taper length is shown in Fig. 4. It is clear that for long taper lengths (≥2 mm) there is a PCE of >99% over the full wavelength range. This relatively large footprint is the main trade-off for targeting broadband performance. It is anticipated that a small footprint will not be as critical as a metric for realizing a MIR waveguide spectrometer compared to SOI photonic devices required for telecommunications. In addition, since a simple linear taper is utilized, it might be possible to reduce the length by up to 40% by optimizing the taper shape while still maintaining adiabatic performance.[41]

C. Broadband TE1 to TE0 mode conversion

The standard approach to converting the higher-order TE1 mode to the fundamental TE0 mode is to phase match by using an asymmetric directional coupler. The disadvantage of using a directional coupler is that it will have inherently narrow-band operation and will also be sensitive to fabrication tolerances. To provide broadband performance that is also fabrication tolerant, the higher-order mode converters proposed by Chen *et al.* were utilized.[42,43] This approach is based on using an asymmetric taper structure that provides a different effective path-length for the anti-phase components of the TE1 mode so that both components become in-phase and a TE0 mode is generated at the output. The higher-order mode converter parameters are optimized to satisfy the following phase matching condition: $\Delta\Phi = 2\pi\Delta L_{eff}/\lambda = \pi$, where $\Delta\Phi$ is the phase change difference of the two anti-phase components and ΔL_{eff} is the effective path difference.

This was modeled by first optimizing a design that contained only two asymmetric tapers (see Fig. S1 of the supplementary material). The input (W_{TE1}) and output (W_{TE0}) width were fixed at 9 μm to ensure that the TE1 mode would be sufficiently far from any mode hybridization region. W_{TE0} was subsequently tapered to 6 μm width over a very short distance (10 μm) to ensure that any fraction of the

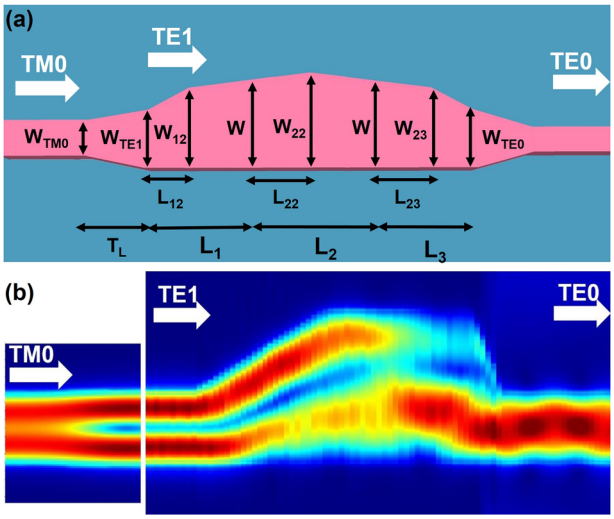

FIG. 5. (a) A top-down schematic diagram of the complete polarization rotator with an adiabatic linear taper that converts from TM0 to TE1 (not to scale), before subsequent higher-order TE1 to TE0 mode conversion by an asymmetric taper structure (see the supplementary material for optimized parameter details). The total length of the optimized polarization rotator structure is 2.22 mm. (b) The simulated light propagation through the optimized polarization rotator with a TM0 injected mode source.

TE1 mode that was not fully converted would be cut-off by operating in single-mode operation. The optimization was performed initially by using the 2.5D variational finite difference time domain (FDTD) method; however, it was found that this led to a large discrepancy when compared to 3D FDTD verification simulations. This discrepancy most likely arises due to the effective modal index error caused when collapsing a rib waveguide structure in the vertical axis.

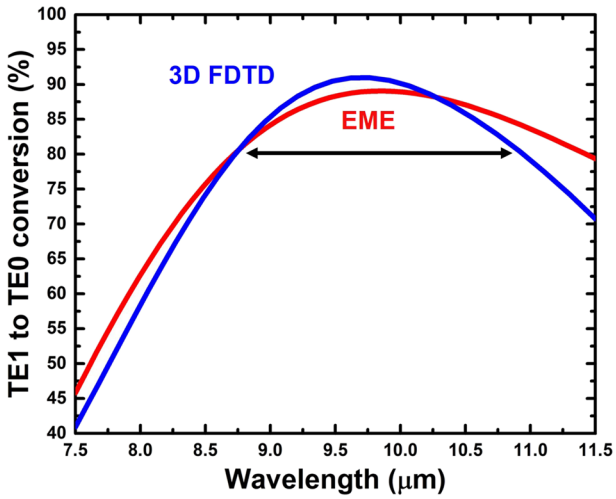

FIG. 6. The simulated TE1 to TE0 conversion efficiency for the optimized higher-order mode converter consisting of six asymmetric tapers modeled with the eigenmode expansion (EME) solver and 3D finite difference time domain (3D FDTD) method. The 1 dB insertion loss point is highlighted by an arrow for the 3D FDTD spectra.

To accurately model within a practical time-frame, the EME solver was implemented via scripting to allow parameter changes in both the width and length. This was then combined with a particle swarm optimization algorithm[44] with the FOM being the power transmitted to the fundamental TE0 mode at W_{TE0}. There were four parameters that were initially optimized, W, L_1, L_2, and L_3, which then subsequently provided parameter bounds for six more complex asymmetric taper structures with parameters W_{12}, W_{22}, W_{23}, L_{12}, L_{22}, and L_{23} [see Fig. 5(a)]. Figure 6 shows the modeled TE1 to TE0 conversion efficiency for the six optimized asymmetric taper structures. There is good agreement between the EME and the 3D FDTD verification simulation. The optimized structure demonstrates a peak conversion efficiency of ~90% at ~9.75 μm wavelength. The structure was optimized for a center wavelength of 9.5 μm, but it is clear that there is an asymmetry over the 8–11 μm range. There is still, however, ≥ 80% conversion over a 2 μm bandwidth (9–11 μm). The complete waveguide polarization rotator design consists of a linear adiabatic taper (TM0 to TE1) followed by an asymmetric taper structure (TE1 to TE0) [see Fig. 5(a)].

III. FABRICATION AND CHARACTERIZATION

A waveguide polarization rotator consisting of an adiabatic 2 mm long linear taper for broadband TM0 to TE1 mode conversion followed by the optimized TE1 to TE0 higher-order mode converter was fabricated using commercially grown Ge-on-Si (IQE Si plc).[27] The waveguides were patterned by electron-beam lithography by using the hydrogen silsesquioxane (HSQ) resist. They were subsequently etched to a target depth of 1000 nm with a mixed gas (SF_6 and C_4F_8) process.[45] A surface profiler was used to measure the actual etch depth (~1030 nm). Residual HSQ was removed using dilute hydrofluoric acid, and subsequently, the waveguides were diced using a diamond saw before optical facet polishing.

The fabricated polarization rotator was characterized using a MIR setup consisting of an external QCL (Daylight Solutions MirCat-QT) package that provides continuous tuning from 7.5 μm to 11.5 μm wavelength with ≥50 mW of output across the range. The QCL was end-fire coupled to the waveguides via a free-space optical setup. A high extinction ratio (≥40 dB) wire grid polarizer was used to ensure that only a TM fundamental mode was excited at the input. At the output, the polarization axis of another identical polarizer was adjusted for the detection of the transmitted TE0 and TM0 modes by recording each spectrum on a liquid nitrogen cooled mercury cadmium telluride detector. An optical chopper was used to modulate the QCL to enable the use of a lock-in amplifier; this reduces the effects of ambient black-body radiation and improves the signal-to-noise ratio (see Fig. S2 of the supplementary material). The QCL was operated in the pulsed mode (5% duty cycle) to increase the effective spectral bandwidth of the source to minimize the effect of cavity resonances that would otherwise be formed between the two waveguide end facets. This is important for the accurate measurement of the PER since the TE0 and TM0 modes have different propagation constants, and this would result in either an over or

under-estimation of the PER depending upon the wavelength (see Fig. S3 of the supplementary material). The PER and IL are defined as

$$PER = -10 \times \log_{10}\left(\frac{TM - TM}{TM - TE}\right), \quad (2)$$

$$IL = 10 \times \log_{10}(TM - TE). \quad (3)$$

Figure 7(a) shows the measured PER as a function of the wavelength. It was found that for wavelengths ≤8.5 μm, the PER rapidly decreased. This was not expected since long tapers were utilized to provide a high PER across the 8–11 μm wavelength range. This decrease in the PER was attributed to a strong background signal originating from a TM excited slab mode at the input (see Figs. S4 and S5 of the supplementary material). Since the polarization of this slab mode is not rotated, this has the effect of artificially decreasing the PER. Due to this effect, the PER was measured from 8.5 μm to 11.5 μm (100 nm increments), where the TM slab modes are cut-off. The difference in propagation loss between the TM0 and TE0 modes (see Fig. 2) was taken into account for the calculation of the PER, but it turned out to be not very significant (see Fig. S6 of the supplementary material). It is clear from Fig. 7(a) that a PER of ≥12 dB was found across the full range, where the peak PER of ~24 dB is located at ~9.1 μm. Figure 7(b) shows the measured IL as a function of wavelength. The IL of the waveguide polarization rotator was measured by comparing the transmittance of eight reference 6 μm wide straight waveguides that had the same overall length (1 cm). A large number of reference waveguides were measured to provide sufficient statistics to account for the uncertainties from both waveguide fabrication non-uniformity and end-fire coupling error. It is evident from Fig. 7(b) that there is quite a significant error with the measured IL, which is expected since errors as large as 1 dB are typical for end-fire coupling with a free-space optical setup.[46] This explains why there is an uncertainty present with the IL measured between 9 μm and 11 μm wavelengths since it is most likely at the limit of what can be accurately measured with the experimental setup. The average IL measured across this range is ~0.85 dB. Taking into account the error on the measurement, it is reasonable to assume that the IL between 9 μm and 11 μm wavelengths is ≤1 dB, which would agree well with the modeling (see Fig. 8, inset).

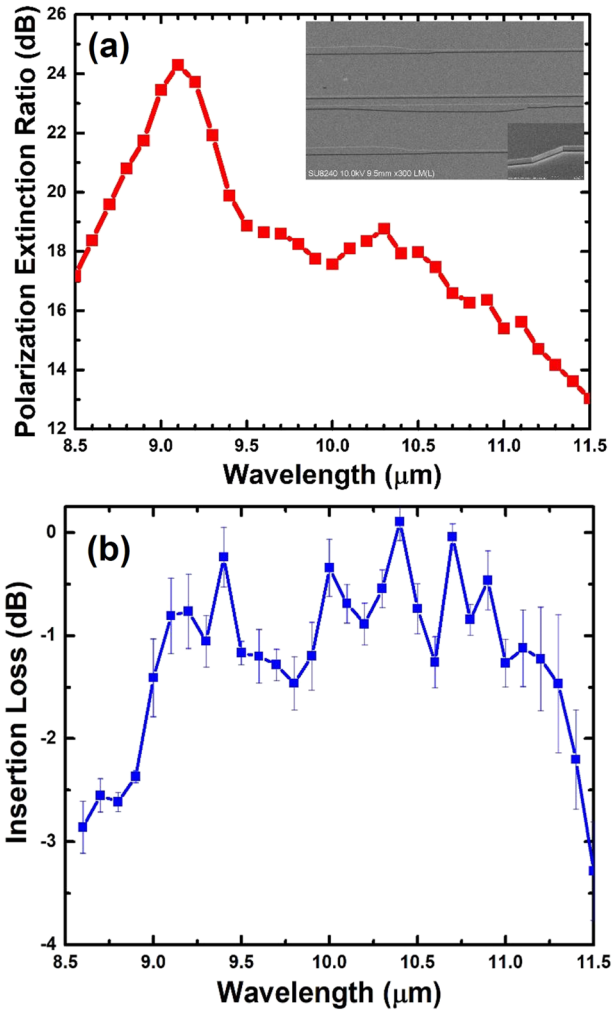

FIG. 7. (a) The experimentally measured polarization extinction ratio (PER) as a function of the wavelength. The inset shows a scanning electron microscope image of the waveguide polarization rotator. (b) The experimentally measured insertion loss (IL) as a function of wavelength for the fabricated waveguide polarization rotator.

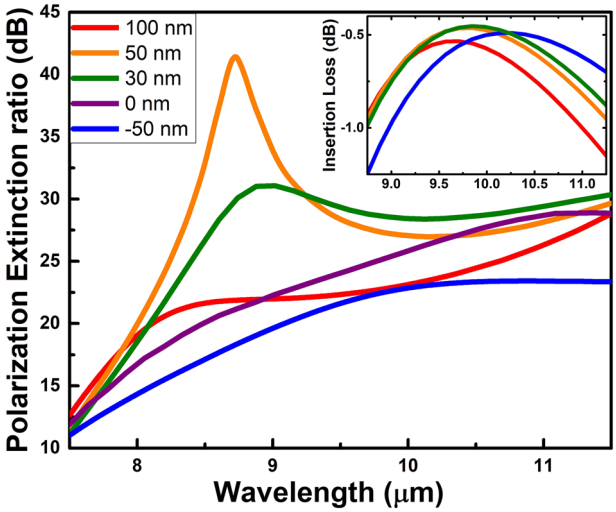

FIG. 8. The modeled polarization extinction ratio vs wavelength for over and under etching compared to the target etch depth of 1000 nm (Δd = 0 nm). The Δd = 30 nm case corresponds to the etch depth achieved with the actual fabricated devices presented within this work. The inset shows the corresponding effect that Δd has on the insertion loss.

IV. FABRICATION TOLERANCE

An important consideration for any polarization rotator is its tolerance to fabrication errors. As this device can be split into two distinct mode conversion regions, the effect of fabrication error can be easily analyzed since the PER and IL are dominated by the TM0

to TE1 and TE1 to TE0 mode converter regions, respectively. Since the experimental results demonstrated an average IL <1 dB and a PER ≥15 dB between 9 μm and 11 μm wavelengths, this will be the comparison for analysis. It is found, as expected, that the design is highly tolerant of lithography errors since it is based on the mode evolution approach and only consists of symmetric and asymmetric tapers. The PER remains largely unaffected even for a width change (Δw) as large as ±250 nm compared to the nominal design. To maintain an IL of ≤1 dB over a 2 μm bandwidth, however, requires that the Δw should be smaller than ±100 nm. This lithography tolerance should be easily achievable within a silicon photonics foundry.[47,48] As electron beam lithography was utilized for the fabrication of the devices presented here, Δw can be assumed to be negligible. What is important is the sensitivity to a change in etch depth compared to the nominal design (Δd). Figure 8 shows the modeled PER as a function of wavelength for the target etch depth of 1000 nm (Δd = 0 nm), actual fabricated devices (Δd = 30 nm), and several other over and under etching conditions. The polarization rotator is especially sensitive to under etching, where $\Delta d \leq -70$ nm would result in zero polarization conversion at the shorter wavelengths since the mode hybridization region is shifted to lower widths than the design. The design is found to be far more tolerant to over etching. What is particularly interesting in Fig. 8 is that over etching can result in an improvement of the peak PER at certain wavelengths where there must be a resonance occurring for the 2 mm long linear taper. This is clearly seen with $\Delta d = 50$ nm, where the modeled PER peaks at ~40 dB at 8.75 μm wavelength. As the fabricated polarization rotators were over etched by ~30 nm in the modeled case, this would provide a peak PER of ~30 dB at 9 μm wavelength, which agrees reasonably well with the experimental results [see Fig. 7(a)]. All of the etching conditions presented provide an IL ≤1 dB over a 2 μm bandwidth (see Fig. 8, inset). Therefore, the tolerance of the device to Δd is thus $-5\% \leq \Delta d \leq 10\%$, which is highly achievable with a controllable etch process such as the one used within this work.

V. CONCLUSION

A Ge-on-Si rib waveguide polarization rotator that operates between 9 μm and 11 μm wavelengths with an average insertion loss <1 dB and a polarization extinction ratio ≥15 dB is presented. The polarization rotator is based on the mode evolution approach in order to convert the fundamental supported TM mode to TE mode. An intermediate polarization conversion between the TM0 and TE1 mode is first achieved by using an adiabatic linear taper that is designed to provide a broadband polarization extinction ratio before subsequent higher-order TE1 to TE0 mode conversion is achieved by an asymmetric taper structure. This higher-order mode converter is optimized by utilizing an eigenmode expansion solver with a particle swarm algorithm. The device is straightforward to realize since it requires no additional waveguide fabrication steps. The fabricated waveguide polarization rotators provide an order of magnitude increase in operational bandwidth compared to previously demonstrated devices. The fabrication tolerance was studied, and it was found to be highly resilient to both lithography (Δw ± 100 nm) and etching error ($-50 \leq \Delta d \leq 100$ nm). This represents the first demonstration of a waveguide polarization rotator in the important molecular "fingerprint" region (6.7–20 μm wavelength) and would enable TE mode operation when integrating quantum cascade lasers on-chip.

SUPPLEMENTARY MATERIAL

See the supplementary material for further details regarding the design of the higher-order TE1 to TE0 mode converter, experimental setup, and calculation of the experimentally measured polarization extinction ratio for the fabricated devices.

ACKNOWLEDGMENTS

This work was supported by the EPSRC, Project No. EP/N003225/1, and the Royal Academy of Engineering, Grant No. RF/201819/18/187. The authors would like to thank the staff of the James Watt Nanofabrication Center for technical support for the micro-fabrication of the devices.

REFERENCES

[1] L. C. Pacheco-Londono, W. Ortiz-Rivera, O. M. Primera-Pedrozo, and S. P. Hernandez-Rivera, "Vibrational spectroscopy standoff detection of explosives," Anal. Bioanal. Chem. **395**, 323–335 (2009).
[2] K. V. Oliver, A. Vilasi, A. Marechal, S. H. Moochhala, R. J. Unwin, and P. R. Rich, "Infrared vibrational spectroscopy: A rapid and novel diagnostic and monitoring tool for cystinuria," Sci. Rep. **6**, 7 (2016).
[3] Y. C. Chang, P. Waegli, V. Paeder, A. Homsy, L. Hvozdara, P. van der Wal, J. Di Francesco, N. F. de Rooij, and H. P. Herzig, "Cocaine detection by a mid-infrared waveguide integrated with a microfluidic chip," Lab Chip **12**, 3020–3023 (2012).
[4] J. Hodgkinson and R. P. Tatam, "Optical gas sensing: A review," Meas. Sci. Technol. **24**, 012004 (2013).
[5] R. V. Rossel, D. Walvoort, A. McBratney, L. Janik, and J. Skjemstad, "Visible, near infrared, mid infrared or combined diffuse reflectance spectroscopy for simultaneous assessment of various soil properties," Geoderma **131**, 59–75 (2006).
[6] J. M. Hollas, *Modern Spectroscopy*, 4th ed. (J. Wiley, Chichester, Hoboken, NJ, 2004).
[7] D. Sorak, L. Herberholz, S. Iwascek, S. Altinpinar, F. Pfeifer, and H. W. Siesler, "New developments and applications of handheld Raman, mid-infrared, and near-infrared spectrometers," Appl. Spectrosc. Rev. **47**, 83–115 (2012).
[8] Y. Yu, X. Gai, T. Wang, P. Ma, R. P. Wang, Z. Y. Yang, D. Y. Choi, S. Madden, and B. Luther-Davies, "Mid-infrared supercontinuum generation in chalcogenides," Opt. Mater. Express **3**, 1075–1086 (2013).
[9] C. Charlton, M. Giovannini, J. Faist, and B. Mizaikoff, "Fabrication and characterization of molecular beam epitaxy grown thin-film GaAs waveguides for mid-infrared evanescent field chemical sensing," Anal. Chem. **78**, 4224–4227 (2006).
[10] J. M. Ramirez, V. Vakarin, C. Gilles, J. Frigerio, A. Ballabio, P. Chaisakul, X. Le Roux, C. Alonso-Ramos, G. Maisons, L. Vivien, M. Carras, G. Isella, and D. Marris-Morini, "Low-loss Ge-rich $Si_{0.2}Ge_{0.8}$ waveguides for mid-infrared photonics," Opt. Lett. **42**, 105–108 (2017).
[11] J. M. Ramirez, Q. Liu, V. Vakarin, J. Frigerio, A. Ballabio, X. Le Roux, D. Bouville, L. Vivien, G. Isella, and D. Marris-Morini, "Graded SiGe waveguides with broadband low-loss propagation in the mid infrared," Opt. Express **26**, 870–877 (2018).
[12] M. Nedeljkovic, J. S. Penades, V. Mittal, G. S. Murugan, A. Z. Khokhar, C. Littlejohns, L. G. Carpenter, C. B. E. Gawith, J. S. Wilkinson, and G. Z. Mashanovich, "Germanium-on-silicon waveguides operating at mid-infrared wavelengths up to 8.5 μm," Opt. Express **25**, 27431–27441 (2017).
[13] A. Osman, M. Nedeljkovic, J. S. Penades, Y. Wu, Z. Qu, A. Z. Khokhar, K. Debnath, and G. Z. Mashanovich, "Suspended low-loss germanium waveguides for the longwave infrared," Opt. Lett. **43**, 5997–6000 (2018).
[14] R. Soref, "Mid-infrared photonics in silicon and germanium," Nat. Photonics **4**, 495–497 (2010).

[15]L. Baldassarre, E. Sakat, J. Frigerio, A. Samarelli, K. Gallacher, E. Calandrini, G. Isella, D. J. Paul, M. Ortolani, and P. Biagioni, "Midinfrared plasmon-enhanced spectroscopy with germanium antennas on silicon substrates," Nano Lett. **15**, 7225–7231 (2015).
[16]J. Frigerio, A. Ballabio, K. Gallacher, V. Gilberti, L. Baldassarre, R. Millar, R. Milazzo, L. Maiolo, A. Minotti, F. Bottegoni, P. Biagioni, D. Paul, M. Ortolani, A. Pecora, E. Napolitani, and G. Isella, "Optical properties of highly n-doped germanium obtained by *in situ* doping and laser annealing," J. Phys. D: Appl. Phys. **50**, 465103 (2017).
[17]R. W. Millar, D. C. S. Dumas, K. F. Gallacher, P. Jahandar, C. MacGregor, M. Myronov, and D. J. Paul, "Mid-infrared light emission >3 μm wavelength from tensile strained gesn microdisks," Opt. Express **25**, 25374–25385 (2017).
[18]M. P. Fischer, A. Riede, K. Gallacher, J. Frigerio, G. Pellegrini, M. Ortolani, D. J. Paul, G. Isella, A. Leitenstorfer, P. Biagioni, and D. Brida, "Plasmonic mid-infrared third harmonic generation in germanium nanoantennas," Light: Sci. Appl. **7**, 106 (2018).
[19]K. Gallacher, A. Ballabio, R. W. Millar, J. Frigerio, A. Bashir, I. MacLaren, G. Isella, M. Ortolani, and D. J. Paul, "Mid-infrared intersubband absorption from p-Ge quantum wells grown on Si substrates," Appl. Phys. Lett. **108**, 091114 (2016).
[20]K. Gallacher, R. W. Millar, V. Giliberti, E. Calandrini, L. Baldassarre, J. Frigerio, A. Ballabio, E. Sakat, G. Pellegrini, and G. Isella, "Mid-infrared n-Ge on Si plasmonic based microbolometer sensors," in *2017 IEEE 14th International Conference on Group IV Photonics (GFP)* (IEEE, 2017), pp. 3–4.
[21]N. Bandyopadhyay, M. Chen, S. Sengupta, S. Slivken, and M. Razeghi, "Ultra-broadband quantum cascade laser, tunable over 760 cm^{-1}, with balanced gain," Opt. Express **23**, 21159–21164 (2015).
[22]A. Malik, A. Spott, E. J. Stanton, J. D. Peters, J. D. Kirch, L. J. Mawste, D. Botez, J. R. Meyer, and J. E. Bowers, "Integration of mid-infrared light sources on silicon-based waveguide platforms in 3.5-4.7 m wavelength range," IEEE J. Sel. Top. Quantum Electron. **25**, 1–9 (2019).
[23]S. Radosavljevic, N. T. Beneitez, A. Katumba, M. Muneeb, M. Vanslembrouck, B. Kuyken, and G. Roelkens, "Mid-infrared vernier racetrack resonator tunable filter implemented on a germanium on SOI waveguide platform invited," Opt. Mater. Express **8**, 824–835 (2018).
[24]M. Nedeljkovic, A. V. Velasco, A. Z. Khokhar, A. Delage, P. Cheben, and G. Z. Mashanovich, "Mid-infrared silicon-on-insulator Fourier-transform spectrometer chip," IEEE Photonics Technol. Lett. **28**, 528–531 (2016).
[25]R. A. Soref, F. De Leonardis, and V. M. N. Passaro, "Scanning spectrometer-on-a-chip using thermo-optical spike-filters or vernier-comb filters," J. Lightwave Technol. **37**, 3192–3200 (2019).
[26]M. Montesinos-Ballester, Q. K. Liu, V. Vakarin, J. M. Ramirez, C. Alonso-Ramos, X. Le Roux, J. Frigerio, A. Ballabio, E. Talamas, L. Vivien, G. Isella, and D. Marris-Morini, "On-chip Fourier-transform spectrometer based on spatial heterodyning tuned by thermo-optic effect," Sci. Rep. **9**, 14633 (2019).
[27]K. Gallacher, R. W. Millar, U. Griskeviciute, L. Baldassarre, M. Sorel, M. Ortolani, and D. J. Paul, "Low loss Ge-on-Si waveguides operating in the 8-14 μm atmospheric transmission window," Opt. Express **26**, 25667–25675 (2018).
[28]U. Grišķevičiūtė, R. Millar, K. Gallacher, L. Baldassarre, M. Sorel, M. Ortolani, and D. Paul, "Fingerprint mid-infrared sensing with germanium on silicon waveguides," in *Conference on Lasers and Electro-Optics* (Optical Society of America, 2019), p. STh1N.2.
[29]D. X. Dai, "Advanced passive silicon photonic devices with asymmetric waveguide structures," Proc. IEEE **106**, 2117–2143 (2018).
[30]K. Goi, A. Oka, H. Kusaka, K. Ogawa, T. Y. Liow, X. G. Tu, G. Q. Lo, and D. L. Kwong, "Low-loss partial rib polarization rotator consisting only of silicon core and silica cladding," Opt. Lett. **40**, 1410–1413 (2015).
[31]V. Vakarin, W. N. Ye, J. M. Ramírez, Q. Liu, J. Frigerio, A. Ballabio, G. Isella, L. Vivien, C. Alonso-Ramos, P. Cheben, and D. Marris-Morini, "Ultra-wideband Ge-rich silicon germanium mid-infrared polarization rotator with mode hybridization flattening," Opt. Express **27**, 9838–9847 (2019).
[32]J. Wang, C. H. Lee, B. Niu, H. Y. Huang, Y. Li, M. Li, X. Chen, Z. Sheng, A. M. Wu, W. Li, X. Wang, S. C. Zou, F. W. Gan, and M. H. Qi, "A silicon-on-insulator polarization diversity scheme in the mid-infrared," Opt. Express **23**, 15029–15037 (2015).
[33]A. Rostamian, J. Guo, S. Chakravarty, H. Yan, C. J. Chung, E. Heidari, and R. T. Chen, "Grating-coupled silicon-on-sapphire polarization rotator operating at mid-infrared wavelengths," IEEE Photonics Technol. Lett. **31**, 401–404 (2019).
[34]C. J. Chung, J. Midkiff, K. M. Yoo, A. Rostamian, J. Guo, R. T. Chen, and S. Chakravarty, "InP-based polarization rotator-splitter for mid-infrared photonic integration circuits," AIP Adv. **9**, 015303 (2019).
[35]C. Alonso-Ramos, S. Romero-Garcia, A. Ortega-Monux, I. Molina-Fernandez, R. Zhang, H. G. Bach, and M. Schell, "Polarization rotator for InP rib waveguide," Opt. Lett. **37**, 335–337 (2012).
[36]Y. H. Fei, L. B. Zhang, T. T. Cao, Y. M. Cao, and S. W. Chen, "Ultracompact polarization splitter-rotator based on an asymmetric directional coupler," Appl. Opt. **51**, 8257–8261 (2012).
[37]M. R. Watts and H. A. Haus, "Integrated mode-evolution-based polarization rotators," Opt. Lett. **30**, 138–140 (2005).
[38]D. X. Dai, J. Bauters, and J. E. Bowers, "Passive technologies for future large-scale photonic integrated circuits on silicon: Polarization handling, light non-reciprocity and loss reduction," Light: Sci. Appl. **1**, e1 (2012).
[39]D. X. Dai and H. Wu, "Realization of a compact polarization splitter-rotator on silicon," Opt. Lett. **41**, 2346–2349 (2016).
[40]Y. L. Yin, Z. Y. Li, and D. X. Dai, "Ultra-broadband polarization splitter-rotator based on the mode evolution in a dual-core adiabatic taper," J. Lightwave Technol. **35**, 2227–2233 (2017).
[41]J. S. Guo and Y. L. Zhao, "Analysis of mode hybridization in tapered waveguides," IEEE Photonics Technol. Lett. **27**, 2441–2444 (2015).
[42]D. G. Chen, X. Xiao, L. Wang, Y. Yu, W. Liu, and Q. Yang, "Low-loss and fabrication tolerant silicon mode-order converters based on novel compact tapers," Opt. Express **23**, 11152–11159 (2015).
[43]D. G. Chen, X. Xiao, L. Wang, W. Liu, Q. Yang, and S. H. Yu, "Highly efficient silicon optical polarization rotators based on mode order conversions," Opt. Lett. **41**, 1070–1073 (2016).
[44]Y. Zhang, S. Y. Yang, A. E. J. Lim, G. Q. Lo, C. Galland, T. Baehr-Jones, and M. Hochberg, "A compact and low loss Y-junction for submicron silicon waveguide," Opt. Express **21**, 1310–1316 (2013).
[45]M. M. Mirza, H. Zhou, P. Velha, X. Li, K. E. Docherty, A. Samarelli, G. Ternent, and D. J. Paul, "Nanofabrication of high aspect ratio (~50:1) sub-10 nm silicon nanowires using inductively coupled plasma etching," J. Vac. Sci. Technol., B **30**, 06FF02 (2012).
[46]G. T. Reed, *Silicon Photonics: An Introduction* (Wiley, 2004).
[47]A. Rahim, T. Spuesens, R. Baets, and W. Bogaerts, "Open-access silicon photonics: Current status and emerging initiatives," Proc. IEEE **106**, 2313–2330 (2018).
[48]A. H. Atabaki, S. Moazeni, F. Pavanello, H. Gevorgyan, J. Notaros, L. Alloatti, M. T. Wade, C. Sun, S. A. Kruger, H. Y. Meng, K. Al Qubaisi, I. Wang, B. H. Zhang, A. Khilo, C. V. Baiocco, M. A. Popovic, V. M. Stojanovic, and R. J. Ram, "Integrating photonics with silicon nanoelectronics for the next generation of systems on a chip," Nature **556**, 349 (2018).